A Detailed Post Mortem Analysis of Solid Oxide Electrolyzer Cells after Long-Term Stack Operation

Carolin E. Frey, Qingping Fang, Doris Sebold, Ludger Blum, Norbert H. Menzler

Institute of Energy and Climate Research (IEK), Forschungszentrum Jülich GmbH
52425 Jülich, Germany

A long-term test with a two-layer solid oxide electrolyzer stack was carried out for more than 20 000 hours. The stack was mainly operated in a furnace environment in electrolysis mode, with 50% humidification of H_2 at 800 °C, a current density of -0.5 Acm^{-2} and steam conversion rate of 50%. After ~18 000 hours of operation in electrolysis mode, the voltage and area specific resistance degradation rates were ~0.6%/kh and 8.2%/kh, respectively. A detailed post mortem analysis of cells including ICP-OES and microstructural analysis was conducted. Two main degradation phenomena were observed in the cells: In the fuel electrode, the depletion and agglomeration of nickel were visible. At the air electrode, demixing of the air electrode and diffusion of strontium took place. This was observed in the formation of strontium zirconate at the interface between the electrolyte and the GDC barrier layer as well as in the formation of strontium oxide and strontium chromate on top of the cells. Strontium oxide was even found in pores on top of the electrolyte.

Introduction

Solid oxide electrolysis cells (SOECs) offer the possibility to convert surplus electricity generated by regenerative sources like wind and solar power directly into hydrogen by water splitting. Thus SOECs may act as key enablers for an energy environment which does not depend on fossile fuels. To introduce SOEC technology onto the market, the lifetime of stacks must be extended. Degradation phenomena must also be identified, understood and eliminated or reduced. Over the last few years, some reports on solid oxide electrolysis stacks have been published (1-9). To our knowledge, only a limited number of studies on the detailed post analysis of a stack have been published so far. In 2017, Rinaldi et al. (10) published test results of an electrolysis stack, which was tested for 10 700 h at -0.5 $A \cdot cm^{-2}$ with a degradation rate of 0.5% kh^{-1}. Post-test analysis of this stack revealed silicon impurities at the fuel electrode interface to the electrolyte and sulfur inclusion along cracks of the oxygen electrode. Nickel depletion at the electrolyte/fuel electrode interface was detected to a depth of 5 µm. There was void formation in the YSZ electrolyte at the grain boundaries next to the GDC barrier layer and formation of $SrZrO_3$ at a new, dense layer at the interface between YSZ and GDC. The air electrode after operation was investigated by Mawdsley et al. in 2009. After 1000 h and 2000 h, Cr substitution in $(La,Sr)CoO_3$ lowered the electrical conductivity of the so-called bond coat, which we would refer to as the chromium retention layer and contact layer, and partial oxygen electrode delamination could be seen (11). Based on these studies, there is a need for further post-test analysis of long-term electrolysis stacks to investigate degradation phenomena and increase the lifetime of SOEC stacks under different working conditions.

Here, we report on an SOEC stack that was operated for more than 18 000 hours in electrolysis mode at -0.5 $A \cdot cm^{-2}$ with a steam conversion rate of 50%, most of the time at 800 °C. The first electrochemical results after 5000 h of operation were described by Fang et al. (12). The electrochemical performance and a preliminary post mortem analysis were presented by Fang et al. (13).

Experimental

The detailed experimental setup of the two-layer F10-design counter-flow stack (internal number: F1002-165) is described in Fang et al. (12) The following table gives a brief overview of the anode-supported cells (ASCs in SOFC mode) and stack components used.

*Table 1: Cell and stack components of the used SOEC stack. *The thickness of the cell frame is adapted to cell thickness and the thickness of the interconnector fits the thermocouples used.*

Function	Material name	Material	Thickness (µm)
Cell frame	Crofer 22 APU	Ferritic steel with ~22% Cr	2500*
Interconnector	Crofer 22 APU	Ferritic steel with ~22% Cr	5000*
Protective coating	MCF	$MnCo_{1.9}Fe_{0.1}O_4$ applied by atmospheric plasma spraying	50-100
Contact coating (+)	LCC 10	$La_1Mn_{0.45}Co_{0.35}Cu_{0.2}O_3$ applied by wet powder spaying	~100
Air electrode	LSCF	$La_{0.58}Sr_{0.4}Co_{0.2}Fe_{0.8}O_{3-\delta}$	~40
Barrier layer	GDC	$Ce_{0.8}Gd_{0.2}O_{1.9}$ applied by physical vapor deposition	~0.5
Electrolyte	8YSZ	$Y_{0.148}Zr_{0.852}O_{1.926}$	~10
Fuel electrode	Ni/8YSZ	Ni + $Y_{0.148}Zr_{0.852}O_{1.926}$	~7
Substrate	Ni/8YSZ	Ni + $Y_{0.148}Zr_{0.852}O_{1.926}$	1000
Contact (-)	Ni mesh	Nickel	1200

Each cell is of a size of 10 cm x 10 cm and has an active cell area of 80 cm^2. The joining, conditioning and characterization procedures have already been described in a previous publication (12). The stack was first investigated in both fuel cell and electrolysis mode to characterize the stack and to evaluate the possibility of comparing the stack performance to former SOFC stacks. Then, it was operated in electrolysis mode with a current density of -0.5 $A \cdot cm^{-2}$ and steam conversion rate of 50% at furnace temperatures of 800 °C, 750 °C and 700 °C, respectively. Different temperatures were used to gain information about the influence of temperature on voltage and area specific resistance (ASR) degradation. A period of fuel cell operation with a current density of 0.5 $A \cdot cm^{-2}$ and fuel utilization rate of 50% was then carried out at 800 °C to check the performance in comparison to the beginning and to other stacks, before long-term electrolysis was initiated at -0.5 $A \cdot cm^{-2}$ and steam conversion rate of 50% for ~12 600 h. In total, the stack was operated above 700 °C for more than 20,000 hours, of which ~18,500 hours were in electrolysis mode. During stationary operation, electrochemical impedance spectroscopy (EIS) measurements were performed regularly under the open cell voltage (OCV) condition. Details on the analysis mode can be found in Fang et al.(13).

For the scanning electron microscopy (SEM) characterization, a ZEISS ULTRA 55 (Oberkochen, Germany) equipped with an energy dispersive X-ray spectroscopy (EDS) system Oxford X-Max (Oxford Instruments, Wiesbaden, Germany) was used. SEM measurements were conducted on the embedded and polished cross sections of the whole embedded stack and cell 1 as well as top views of cell 1.

Results and discussion

Electrochemical results

The electrochemical characterization was described by Fang et al. (13). The main results will be summarized briefly in this section. The stack was operated:

- From start until ~ 6,500h in electrolysis mode (region 1)
- From 6,500h until ~ 8,000h in SOFC mode (region 2), and
- From 8,000h until the shut down at about 21,000h again in SOEC mode (region 3)

The average ASR degradation rates in the first electrolysis operation (region 1) at three different temperatures (800, 700, 750°C) were ~10% kh^{-1}, though the difference in voltage degradation was

larger. During the long-term electrolysis (region 3), the voltage and ASR degradation rates of the first 10 000 hours were ~0.4% $kh^{-1}$and 2.7% kh^{-1} respectively. After this, a slower voltage degradation related to a leakage in the test bench was observed. The overall degradation rates of the stack during complete operation (from region 1, 2 and 3) of ~21 000 h were 0.6% $kh^{-1}$and 8.2% $kh^{-1}$for the voltage and ASR degradation at 800 °C, respectively. Impedance measurements and an analysis of the distribution of relaxation times (DRT) revealed the increasing ohmic resistance as the main degradation mechanism. This was most probably caused by a decrease in the conductivity of the fuel electrode. In the preliminary post-test analysis, this was found to be related to the depletion of nickel in the fuel electrode function layer. There was also an increase in the polarization of the air electrode. An extensive post-test characterization to analyze the cause of the observed phenomena is performed in this paper.

Stack dissection

After operation in electrolysis mode for over 18 000 h, the stack was shut down due to the increased internal leakage rate, mainly in layer 2. One third of the stack was then embedded in resin and the rest was disassembled according to our internal protocols (14) for visual inspection. The following degradation could be observed while disassembling:

1.) Severe degradation caused by burning at layer 2 at the manifold of “air out/fuel in” was found (see Fig. 1). As a consequence, a certain amount of hydrogen was consumed before entering the cell. Between the cell and the cell housing, a metallic foil prevents the glass sealing from blocking the air channels. This foil is uncoated, as it is too thin for plasma coating. It was measurably melted due to heat from the burning, causing a partial blockage of the air channels underneath.

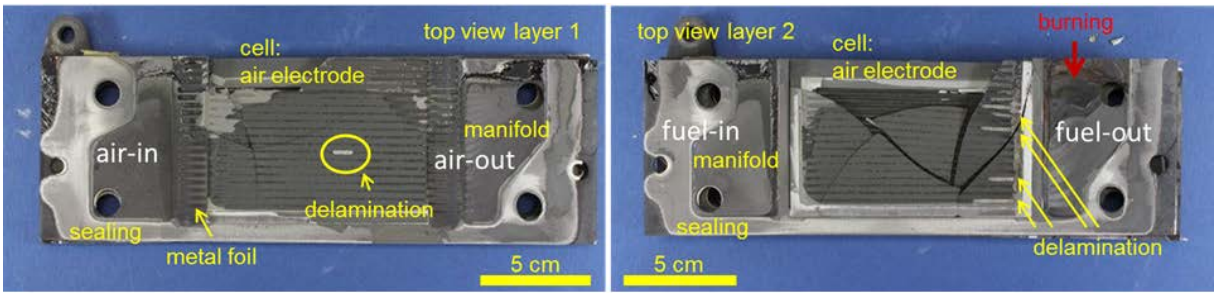

Figure 1: Left: Top view of layer 1 of the SOEC stack during the disassembling. The cell components are labeled. Right: Layer 2 of the SOEC stack during the disassembling. Signs of burning at the manifold are marked by the red arrow. The smaller yellow arrows indicate the delamination of the air electrode.

2.) Both cells were cracked when the stack was opened, but should have remained intact during the stack operation. If this was not the case, there would have been signs of burning or reoxidation on the cells or interconnectors.

3.) There is partial delamination of the air electrode, sometimes also including the barrier layer. The delamination can be found, for example at “air out/fuel in” of cell 2 and in the middle of cell 1 (see Fig. 1). The cause of delamination – SOEC operation or plane-by-plane removal – could not be identified during stack dissection.

4.) The stack was examined with respect to gas tightness according to our internal protocols (15). The glass sealings and interconnectors remained gas tight during the experiment. The leakage test at room temperature after the test and before post mortem analysis showed that the external gas tightness still fulfilled the requirements for new stacks.

Wet chemical analysis

Chemical analysis via ICP-OES (inductively coupled plasma - optical emission spectrometry) was conducted mainly to analyze the chromium content of the cells. Three samples measuring 1 cm^2 were laser cut from cell 1 (the cell without burning damage) at the air inlet, in the middle of the cell and at

the air outlet. The air electrode and afterwards the complete cells were dissolved and investigated via ICP-OES. Detailed information on chromium quantification after fuel cell operation by ICP-OES can be found in the literature (16). The analysis gave the following results:

Table 2: Chromium content of cell 1 at different positions.

Location	Air inlet	Mid cell	Air outlet
Cr [µg cm^{-2}]	67 ± 1	12 ± 1	11 ± 1

Higher amounts of chromium were accumulated at the air inlet side. In the middle of the cell and at the air outlet, not much chromium was observed. We suspect that the major source of the chromium evaporation is the uncoated metal foil in front of the cell, covering the air channels. Chromium species were introduced by the air flow and deposited on the air electrode at the air inlet side. The rest of the cell shows only little impurities of chromium, which proves that the dense manganese-cobalt-iron-spinel (MCF, see Table 1) chromium retention layer, applied by APS, works well in SOEC operation. However, the uncoated thin foil, designed to hold the sealing glass in position, needs to be optimized (cf. Fig. 1 left "metal foil").

Microanalysis via SEM/EDS

An overview of the cell geometry is given in Fig. 2. In this SEM micrograph, the porous substrate and the fuel electrode are visible. On top is a dense electrolyte layer of ~10 µm. The barrier layer (~ 1µm) on top of the electrolyte serves as a diffusion barrier to the air electrode above (see also Fig. 5). The cell is connected to the interconnector by a contact layer. Air channels are left out to secure gas flow above the cell.

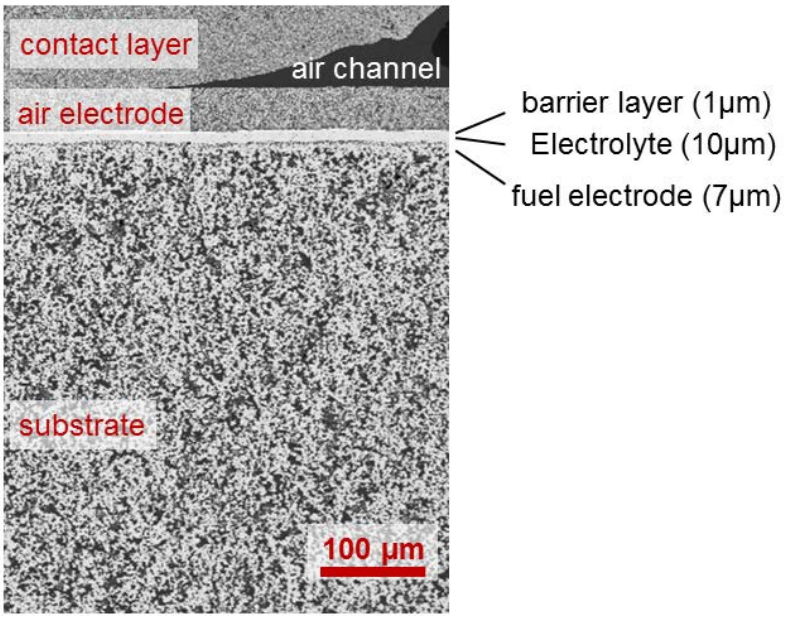

Figure 2: SEM micrograph overview of the cell geometry. From bottom to top: substrate, fuel electrode, electrolyte, barrier layer, air electrode, contact layer/air channel.

The micro-analysis of the cells is split into two parts due to the burning at layer 2. The burning caused damage, which does not help us to understand degradation processes in normal operation. The cause of the burning has to be identified and eliminated in further experiments. The changes in layer 2 caused by the burning are first discussed, followed by layer 1 and phenomena visible in the complete stack. The latter findings are of greater interest because they can be used to improve general stability of the cells.

Investigation of layer 2 – effects of the burning

Fig. 3 shows a SEM micrograph of layer 2 near “air out/fuel in”. Massive degradation was detected in the electrolyte, as well as in the air electrode. The barrier layer as well as parts of the air electrode show cracks and formed new phases. The contact layer (cf. Table 1) also reacted and shows roundly shaped particles measuring a few microns. The degeneration can be linked to the observed phenomena originating from burning at the manifold. For a more intensive analysis, the cell was investigated by EDS.

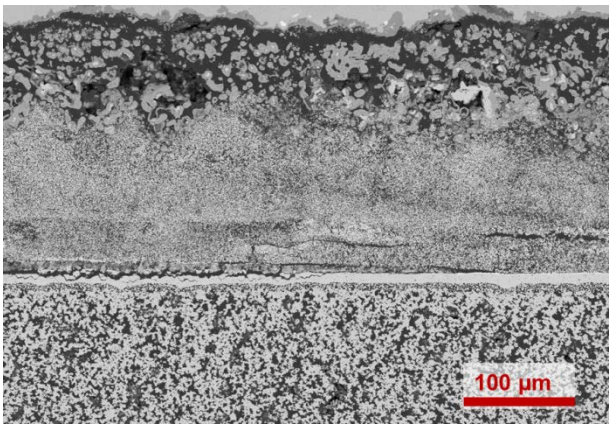

Figure 3: SEM micrographs of cell 2 near “air out”. Depletion of nickel in the fuel electrode, cracks in the electrolyte, delamination of the air electrode and massive degradation of the contact layer are visible.

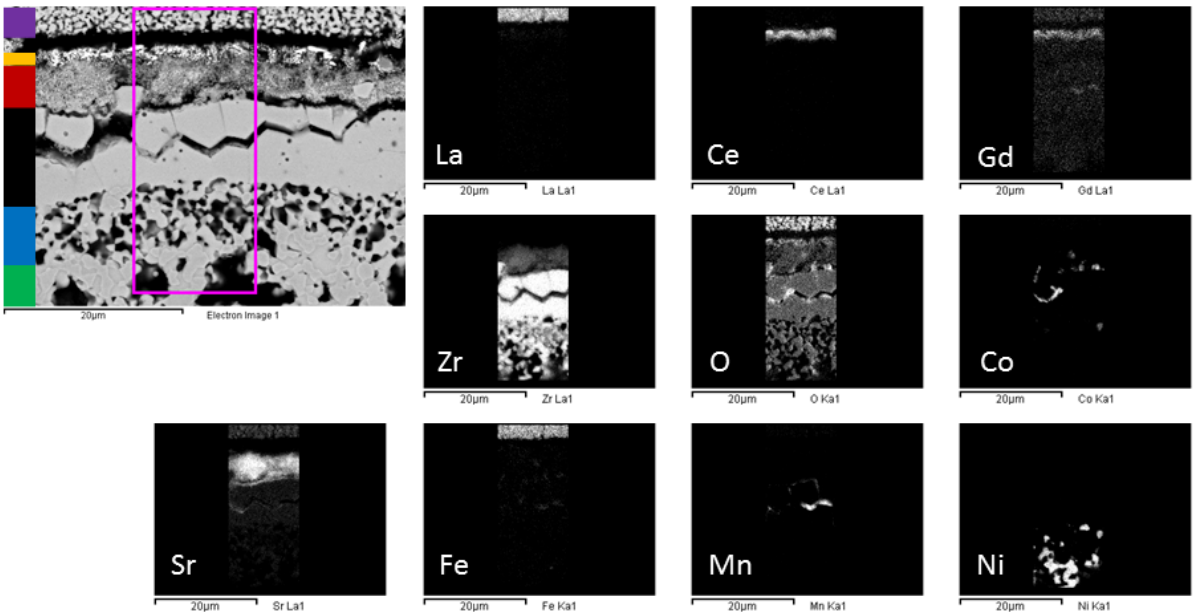

Figure 4: SEM micrograph and EDS mappings of the degradation around the electrolyte in layer 2 near “air out”. The layers are marked by colored lines on the side of the figure: dark green: substrate, blue: fuel electrode functional layer, black: electrolyte, red: newly formed layer, orange: former GDC barrier layer, violet: air electrode.

The elemental mappings (Fig. 4) show the air electrode on top, the GDC barrier layer, the electrolyte, the fuel electrode and parts of the substrate. The air electrode in this analysis appears to have no or little amounts of strontium and cobalt. The decomposition of LSCF has also been previously reported in the literature (17). The missing strontium can be found underneath the cracked GDC barrier layer in the form of very porous strontium zirconate. This is a well-known degradation phenomenon and occurs without a dense barrier layer (18, 19). Directly above and in cracks in the electrolyte, manganese oxide

was formed. In former works concerning SOFC, manganese oxide was found in electrolytes and even in the fuel electrode (15, 20). Manganese is highly mobile under operation conditions as it moves along the grain boundaries and surfaces. In this case, the manganese originates presumably from the LCC10 contact layer (15). The migration of manganese could be the cause or the consequence of the burning at "air out". Co_3O_4 was also found near the electrolyte and in cracks in the electrolyte. It can even be seen in a spot in the fuel electrode. However, in the original air electrode, no or little cobalt was visible. The formation of Co_3O_4 was described by Mahmood et al. and was attributed to depletion of strontium (21). Once the cobalt oxide has formed, it seems to be as mobile as the manganese. In conclusion, the perovskite structure is most likely decomposed. The cause of the degradation is the burning near this spot. It cannot be detected at other locations in the air electrode. Therefore, this result is not as important as other observations described in subsequent parts of this publication.
The composition of the electrolyte remained mostly unchanged. In the fuel electrode, nickel depletion was visible, so that no nickel was found directly beneath the electrolyte.

Investigation of layer 1 – effects of normal operation mode

Degradation of the air electrode and the electrolyte

The air electrode was examined on cell 1 in two ways by SEM: from a top view of the cell and a top view of the embedded and polished cross sections.
The cross sections revealed pores in the GDC barrier layer and directly underneath traces of $SrZrO_3$ in the electrolyte. This phenomenon is visible over the complete cell. Red arrows in Fig. 5 mark an example of the formation of $SrZrO_3$ near "air in". Cracks in the air electrode (some of them marked by yellow dots) resulted most probably from the preparation of the cross sections, because they cannot be found at the weakest points in the air electrode material.

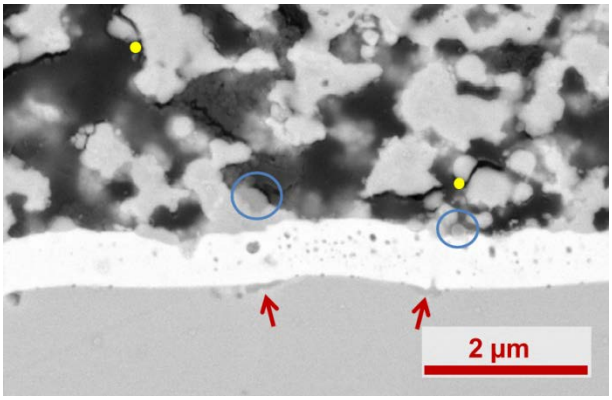

Figure 5: SEM micrograph showing pores in the GDC barrier layer and $SrZrO_3$ (marked by red arrows) in the electrolyte underneath near "air in".

Strontium zirconate forms according to the literature (17, 22) in the sintering process. We did not find a continuous layer of strontium zirconate in this cell and therefore do not conclude any significant contribution to the increase in the ohmic resistance.
The different gray shades of the air electrode (marked in blue) could not be assigned to a phase change within the detection limit of the EDS, but they could be LSCF of a slightly different elemental composition.

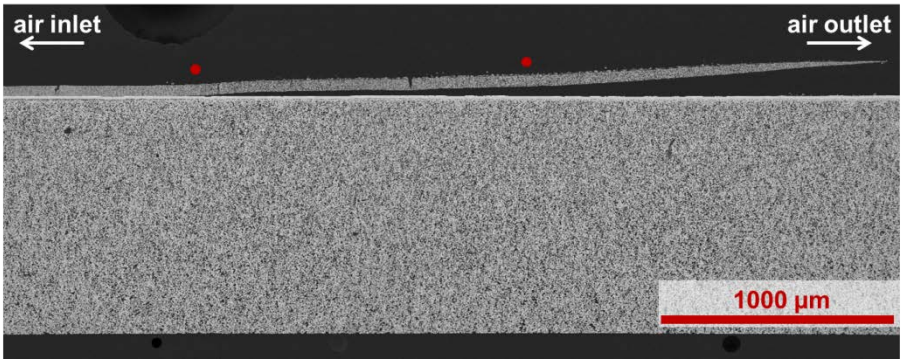

Figure 6: SEM micrograph of the delamination of the air electrode near "air out" of layer 1. The red marks indicate the locations of higher magnification, shown in Fig. 7.

At the air outlet of cell 1, delamination of the air electrode was found over approximately 2.8 mm (see Fig. 6). All the following changes become more pronounced in the direction of the air outlet at this spot.
1.) On top of this delaminated part, $SrCrO_4$ particles were found, which become larger in the direction of "air out".
2.) Needles of $SrCrO_4$ were found in the air electrode. There are more and larger needles towards the end of the cell (air outlet).
3.) The microstructure of the air electrode alters. It becomes more porous and particles are larger and smoother than in the direction of "air in".
4.) The visible vertical cracks arise during cathode paste drying and do not influence cell performance
Figure 7 shows the degradation phenomena. For comparison, a SEM micrograph is also shown with "normal" air electrode microstructure near the delamination (Figure 7, right). Analyzed with EDS, there is less strontium, but more lanthanum in the air electrode at the direction of "air out". The electrolyte and the GDC barrier layer underneath the delaminated part remained completely intact.

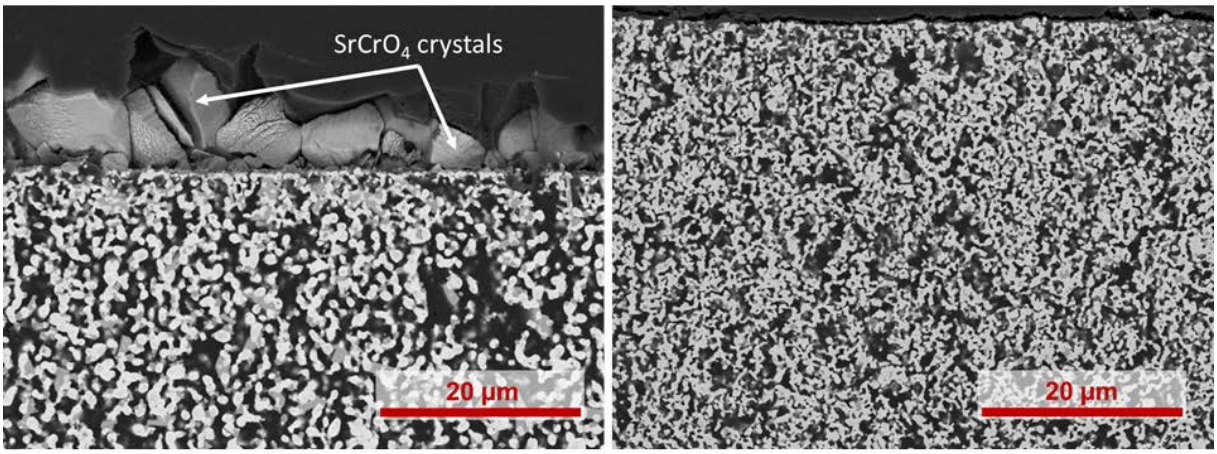

Figure 7: SEM micrograph of the air electrode near "air out". Red spots in Fig. 6 indicate the location of both micrographs. Left: large particles of $SrCrO_4$ were formed on top of the air electrode and needles of $SrCrO_4$ in the air electrode. Right: for comparison, air electrode at the beginning of the delamination in the same magnification.

The degradation of the air electrode at the air outlet is most probably caused by the Crofer 22 APU uncoated metal foil located at the end of the cell directly at "air out". The diffusion of chromium from the foil at the end of the cell leads to the formation of the strontium chromate on top and in the cells. With respect to the formation of $SrCrO_4$ (proved by EDX point analysis) there is less strontium in the air electrode and the morphology started to change as explained above. Such strong degradation could only be found on a small part (approximately 2 mm) at the end of the cell. This results from the diffusion of chromium along the chromium partial pressure and against the air flow in the cell. At the air inlet, strontium chromate was also found. As the diffusion takes place along the gas flow, a broader

distribution of the chromate over the cell is visible and degradation is not concentrated at one particular point. However, if analyzed over a certain area, there is higher chromium content at “air in” than at “air out”. In conclusion, more chromium is transported with the gas flow than against it.
In any case, the metal foil needs to be modified to ensure that no or less chromium diffuses onto the cell. This can be done with a replacement, e.g. with Al_2O_3 forming steels, using a ceramic foil instead of a metallic one or the application of a chromium retention layer as used for the cell housing and interconnectors.
The phenomenon of delamination of the air electrode during electrolysis operation is well known for LSM ($La_{0.65}Sr_{0.3}MnO_{3-d}$) electrodes, but not for LSCF (23). There are three possible scenarios leading to the degradation:
1. Structural changes caused by the formation of strontium chromate weaken the attachment between GDC and the air electrode which is detached because of the change in microstructures.
2. The air electrode was already detached by friction occurring during the sintering process and the degradation is severe due to the position of the detached anode directly next to the metal foil.
3. Due to the increased internal pressure between the electrolyte and air electrode in electrolysis operation, local cracking can occur and lead to the delamination of the air electrode (24). The position of the air electrode directly next to the metal foil promotes the formation of strontium chromate.
The SEM micrograph (top view) of the air electrode of cell 1 shows cracks in the electrode and the reaction of strontium (see Fig. 8).

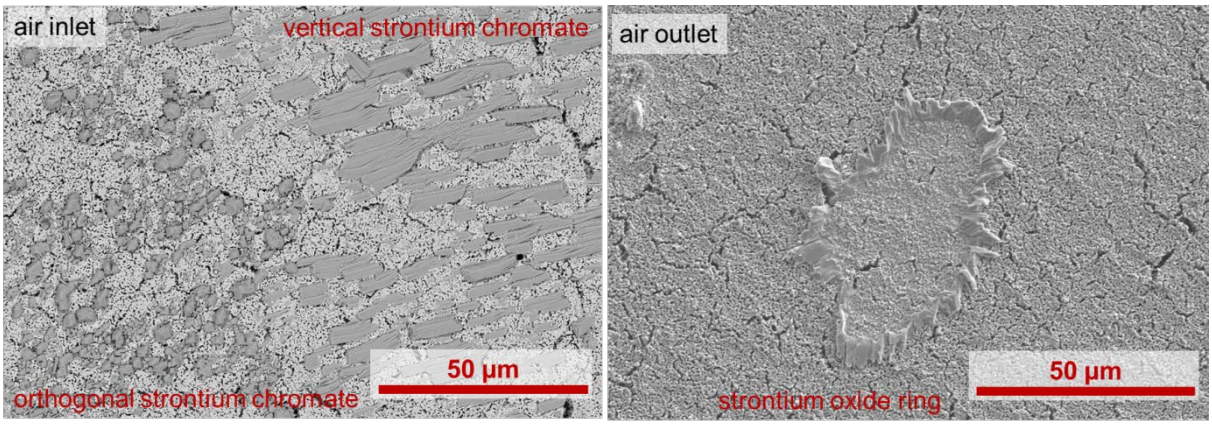

Figure 8: SEM micrograph top view of the air electrode. Left: the air inlet shows strontium chromate; Right: ring of strontium oxide on top of the electrode at the air outlet.

Near “air in”, high amounts of strontium chromate in the form of needles were found. Some of the needles were located on top of the electrode, some of them were partially inside and oriented orthogonally to the deposited chromate. Near “air out”, rings of strontium oxide were found on top of the cell. As stated previously, chemical analysis showed that chromium can also be found in higher amounts at the air inlet than at the air outlet. This phenomenon has been shown before: strontium chromate is more likely to form at the air inlet than at the air outlet (25). Additionally, LSCF is obviously not stable over 18 000 hours in electrolysis mode and strontium diffuses into the electrolyte as well as to the top of the cell. The decomposition of LSCF in electrolysis was also observed in earlier work (18, 26). Detailed information is given in one of the next sections.

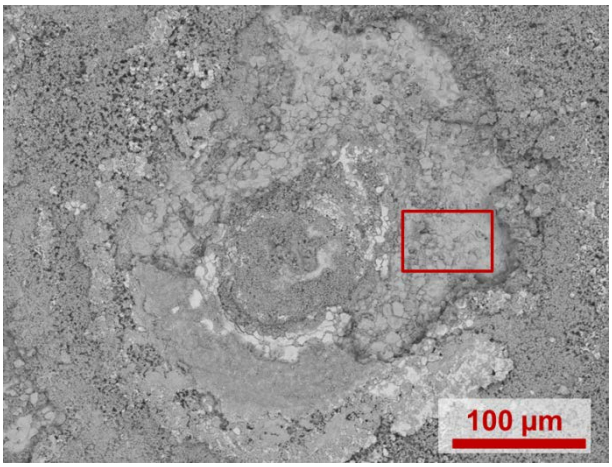

Figure 9: SEM micrograph (top view) of one of the pores in layer 1. Overview of the pore. The red box shows the location of Fig.10.

The surface of the cell of one of the pores in the middle of cell 1 (see Fig. 9) was investigated by SEM/EDS. A pore in this case refers to a spot at the cell, where detachment of at least one layer took place. This pore was not affected by the burning and therefore only shows degradation caused by time and temperature. Delamination of the air electrode in various states was found in the pores. Figure 10 shows one of the strongest degradation phenomena found for these pores.

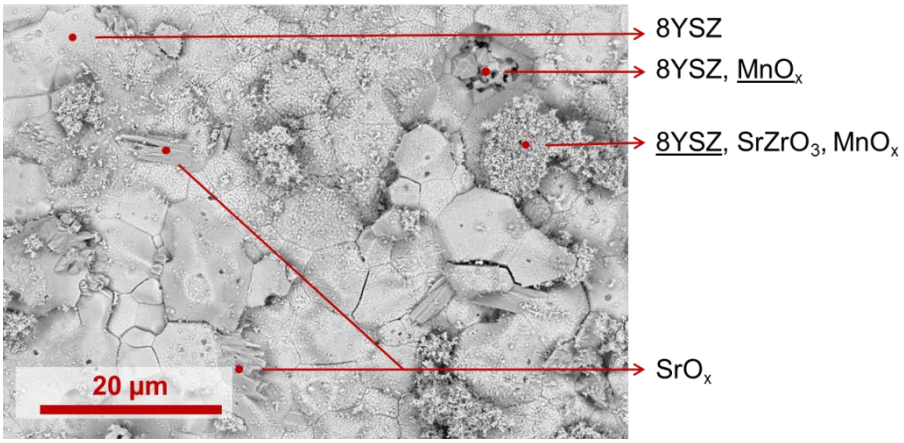

Figure 10: SEM micrograph top view of one of the pores in layer 1. This micrograph shows the strongest degradation phenomena found for those cells. Underlines mark the main species.

The air electrode is completely detached and the electrolyte is visible in most of the image. At the electrolyte, grain boundaries are visible. A hole in the electrolyte can be seen at the upper right corner. EDS measurements confirm that there is not only 8YSZ but also manganese oxide at this spot. Manganese could be the cause for the complete void formation in the electrolyte and was found at other parts of the pores as well. The deeper spot may be still the broken electrolyte, but could also be the beginning of the fuel electrode. The presence of manganese indicates that the pore formation is part of the degradation process in operation.

There are needle-shaped particles on top of the electrolyte. EDS measurements identified the needles as a strontium oxide. Larger agglomerates of nano-sized particles consist of strontium zirconate and the underlying 8YSZ can also be seen. To the knowledge of the authors, the combination of the two strontium-containing species has never been found directly on top of the electrolyte before. The formation of strontium oxide and strontium chromate is more pronounced according to Laurencin et al. (27) in SOEC mode than in SOFC mode. This was explained by the anodic polarization of the LSCF material, which favors the formation of low oxygen vacancies. A high amount of oxygen thus facilitates

the demixing of the air electrode material and leads to the formation of strontium oxide on the electrode (27). In contrast to the SEM micrographs of the cross sections, no strontium chromate can be seen. We conclude that the protective MCF coating works well as a chromium retention layer.
The GDC barrier layer is not visible with EDS analysis. Although the layer only has a thickness of 0.5 µm, cerium and gadolinium should be visible, as at other parts of the pore.
Manganese and strontium in the form of strontium oxide and strontium zirconate are found not only at this spot, but also in other parts of the pore. We would like to present two theories for the formation of the pores:
1.) Since the delamination process leaves a blank electrolyte, major leakage in the GDC barrier layer could lead to the formation or nucleus growth of strontium zirconate underneath the layer. It has been proven that $SrZrO_3$ forms at temperatures of 800 °C (17, 28). The density of strontium zirconate is slightly lower than that of 8YSZ and the volume expansion may lead to cracks and more strontium zirconate being formed. Finally, the delamination of the GDC barrier layer occurs. The post-test analysis could not resolve whether the air electrode delamination occurred due to mechanical stress during operation or during stack dissection.
2.) The formation of manganese oxide could be the cause of the detachment of the air electrode. The diffusion of manganese was proven to occur along grain boundaries or a surface even inside a dense GDC layer (20, 29). Precipitation between the electrolyte and the GDC layer or inside the electrolyte would explain the observed delamination and void formation inside the electrolyte.
At layer 2, various pores can be found near “air out”. This indicates a correlation between the burning at the manifold and the observed voids.

In summary, there is pore formation and delamination of the air electrodes in some parts of the cells, as well in layer 1, which was not affected by the burning, and also in layer 2, especially near the area burnt. Only parts of the cell appear to be affected, but it could explain the burning in layer 2, where a part of the cell, including the electrolyte, was completely destructed.

Nickel agglomeration and depletion

According to the literature, the main degradation mechanism in electrolyzer cells is the agglomeration and depletion of nickel (30-32). As reported in (13), this phenomena is also visible in both cells in this stack. Figure 11 shows a SEM micrograph overlaid with an EDS mapping of nickel (red) and 8YSZ (green). At “fuel out” (Figure 11 left), the depletion of nickel is not as pronounced as at “fuel in” (Figure 11 right). For better comparison, a white line has been added, to visualize more pronounced the part of more or less intact nickel/8YSZ material.
Additionally, the nickel particles in the substrate are coarser. This is caused by the agglomeration of nickel and has been observed before (33, 34). In the DRT analysis, the first peak corresponding to the gas diffusion in the anode substrate decreased with operating time (16). This agrees very well with the higher porosity and the agglomeration of nickel in the cell.

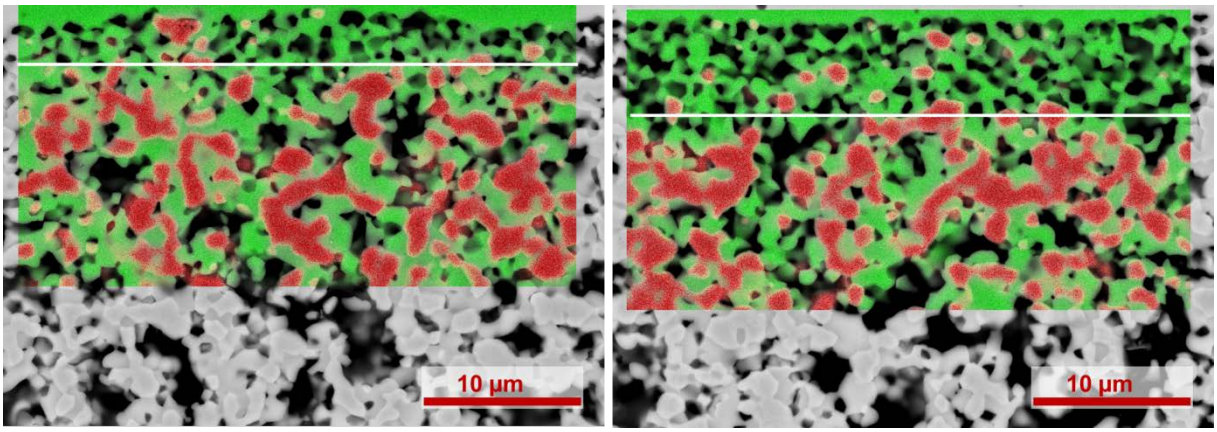

Figure 11: SEM micrographs and EDS mapping of the fuel electrode; left "fuel out", right "fuel in". EDS mapping: in green 8YSZ and in red Ni. The white line marks the area, where the authors see the line of nickel.

The nickel depletion in the stack has already been described by Fang et al. (13), but will be discussed in the following section in detail for completeness. Fig. 12 shows SEM micrographs of the operated cell. The electrolyte is marked in black, the original fuel electrode in blue on the right-hand side and the unaffected substrate in dark green. Additionally, the porous layer, which is caused by nickel depletion is marked in yellow and a denser layer directly beneath in light green. The porosity of the porous layer, the dense layer and the substrate were investigated via ImageJ (porosity) at three different locations on both cells. The width of the porous layer was determined by analySIS (image analysis software tool for measuring porosities, thicknesses etc., Olympus Soft Imaging Solutions GmbH). The mean values and variance of the results of more than 9 locations each are displayed in Table 3 and 4.

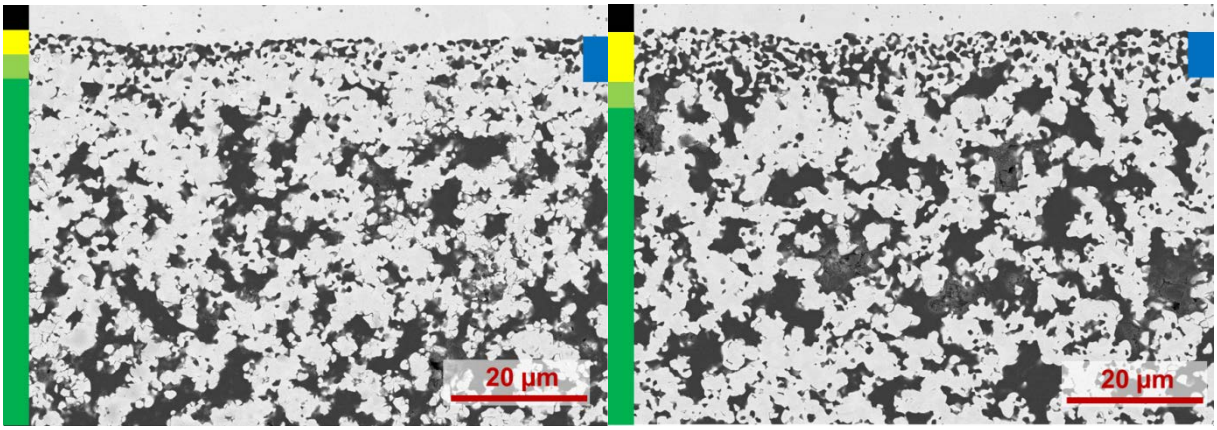

Figure 12: SEM micrographs of the fuel electrode; left "fuel out", right "fuel in". The layers are marked by colored lines on the side of the figure: dark green: substrate, light green: dense layer, yellow: porous layer, black: electrolyte, blue: fuel electrode functional layer.

Table 3: Porosity of the fuel electrode and substrate. The star marks the part where the dense layer is located in the substrate of the cell.

location	Fuel out	Mid cell	Fuel in	Expected values
substrate	38 ± 1 %	38 ± 3 %	39 ± 3 %	~35%
dense layer	18 ± 2 %	19 ± 1 %	33 ± 3 %*	20%/35%*
porous layer	36 ± 3 %	42 ± 1 %	45 ± 2 %	~20%

Table 4: Thickness of the porous layer.

location	Fuel out	Mid cell	Fuel in
Width of the porous layer	3.0 ± 0.2 µm	3.7 ± 0.3 µm	6.7 ± 0.6 µm

The porosity of the substrate is expected to be approximately 35% (35). The substrate of the cells shows a slightly higher value, but is within the range of normal values. Variances can also be explained by the agglomeration of nickel (see also Fig. 11). The porosity of the fuel electrode near the electrolyte is between 36-45% and increases from “fuel out” to “fuel in”. The values are above the expected porosity of ~20% for the pristine reduced fuel electrode (35). The higher porosity of the fuel electrode functional layer has been observed before and was interpreted as the depletion of nickel (18, 36). The width of this layer also increases in the direction of the fuel inlet. Particularly at “fuel in”, the thickness of the porous layer is doubled and reaches the overall fuel electrode thickness of ~7 µm.
The difference in Ni depletion can be explained by the composition of the gaseous atmosphere at the various points. At “fuel in”, there is a high amount of steam and a relatively low amount of hydrogen. In contrast, the fuel gas at the fuel outlet comprises higher amounts of hydrogen. Therefore, the atmosphere at the fuel inlet is oxidizing in comparison to “fuel out”. Nickel is transported via nickel hydroxides, particularly at places with a higher oxidation potential and steam concentration, for example at “fuel in” (36). Further thermo-chemical characterization and calculations are currently being prepared to investigate this further.
At “fuel out” and in the middle of the cell, there is a dense layer directly next to the described porous one, facing the substrate. This is the place where the nickel appears to re-condense. This phenomenon leads to a special shift of the triple-phase boundary and an enlargement of the electrolyte thickness, leading to higher ohmic resistance in the stack. As described by Zheng et al. (37), the resistance does not increase linearly but even more with porous ionic conductors. Therefore, the greatest increase in ohmic resistance can be assigned to the depletion of nickel, as stated by Fang et al. (13). This is particularly pronounced for the cells at the fuel inlet and in the middle of the cell. At “fuel in”, this layer is located in the substrate. With a porosity of about 33%, this dense phase is also denser than the substrate was before. However, the dense layers are not as thick as the part where nickel depletes. There are two possible explanations for this:
1.) Nickel is more equally distributed in the neighboring substrate. 2.) As reported in the literature, nickel simply depletes out of the cell.
The depletion of nickel is the main reason for the observed increase in ohmic resistance. The subsequent formation of a porous 8YSZ layer leads to a thickness increase of the ion conductor.

Comparison to former results and to operation in SOFC mode

At the beginning of this publication, different post-test analyses were introduced. In the fuel electrodes, the change in nickel morphology and the depletion of nickel were observed (10). Rinaldi et al. (10) also identified the formation of strontium zirconate in their stack. Delamination of the air electrode, as described by Mawdsley et al. (11), was found in very few parts of the cell. In our stack, this is caused by a missing chromium retention layer on an uncoated foil covering the air channels to retain the glass sealing. In contrast to these studies, no impurities of sulfur or silicon were observed (10).
In comparison to stacks operated in SOFC mode, two degradation phenomena are obviously accelerated: nickel depletion and demixing of the LSCF air electrode. A stack operated 19 000 h at 800°C and 0.5 $A \cdot cm^{-2}$ in SOFC mode showed no or almost no depletion or agglomeration of nickel (29). Laurencin et al. described the demixing of the air electrode as more severe in SOEC mode than in SOFC mode (27). As a conclusion, the two electrode materials need to be adjusted to SOEC mode and cannot simply be transferred from cells in SOFC mode. For future stacks, an alternative air electrode material would be an option to prevent the diffusion of strontium. The depletion of nickel is a problem, which also has to be addressed. Microstructural changes could improve the stability of nickel in the cell. However, former results indicate that this might not be a promising approach (38). The development of a new fuel electrode catalyst may therefore be necessary.

Conclusion

A stack operated for over 18 000 h in electrolysis mode was post-test analyzed using SEM, EDS and ICP-OES. In this stack (internal number: F1002-165), different changes were observed in the cells. On the one hand, we found phenomena, which were visible over the complete cells. This includes the depletion of nickel and the demixing of the air electrode. The demixing of the air electrode leads to the segregation of strontium, which is visible in the formation of strontium zirconate at the interface between electrolyte and the GDC barrier layer as well as in the formation of strontium oxide and strontium chromate on top of the cells. On the other hand, phenomena were found, which were only located at some spots on the cells: 1.) the formation of pores on the cells, which can be caused by the formation of manganese oxide or strontrium zirconate at the interface between the GDC barrier layer and the electrolyte, 2.) the delamination of the air electrode accompanied by the extreme formation of strontium chromate on top of the cells and 3.) the degradation of one cell, caused by the burning at “air out”/“fuel in”.

The massive increase in ohmic resistance, which was observed for this stack (13) can be attributed to the depletion of nickel in the fuel electrode and therefore to a new porous electrolyte layer between the functional fuel electrode and the dense electrolyte. Additionally, the gas diffusion polarization in the air electrode of layer 2 was significantly increased after ~18,000 h (13). In this post mortem analysis, it was shown that burning was the origin of this degradation, as it led to blocked air channels.

Nickel depletion and the demixing of the air electrode are more significant in SOEC stacks than in SOFC stacks and are the main reasons for the degradation of the cell in “normal” operation mode. Therefore, the electrode materials must be improved before being used further in SOEC stacks.

Acknowledgments

The cooperation with all colleagues working on SOC topics at Forschungszentrum Jülich is greatly acknowledged. The authors would like to thank in particular all colleagues in the FOB department at the IEK-3 for maintaining the endurance test and Dr. Carole Babelot atZEA-1 for conducting the post mortem analysis of the stack.

1. T.-L. Liu, C. Wang, S.-J. Hao, Z.-Q. Fu, B. A. Peppley, Z.-M. Mao, J.-L. Wang and Z.-Q. Mao, *Int. J. Hydrogen Energy*, **41**, 15970 (2016).
2. Y. Zheng, Q. Li, T. Chen, C. Xu and W. G. Wang, *Journal of Power Sources*, **274**, 736 (2015).
3. C. M. Stoots, J. E. O'Brien, K. G. Condie and J. J. Hartvigsen, *Int. J. Hydrogen Energy*, **35**, 4861 (2010).
4. S. D. Ebbesen, J. Høgh, K. A. Nielsen, J. U. Nielsen and M. Mogensen, *Int. J. Hydrogen Energy*, **36**, 7363 (2011).
5. K. Chen and S. P. Jiang, *Int. J. Hydrogen Energy*, **36**, 10541 (2011).
6. K. Wonsyld, L. Bech, J. Ulrik Nielsen and C. Friis Pedersen, *Operational Robustness Studies of Solid Oxide Electrolysis Stacks* (2015).
7. X. Zhang, J. E. O'Brien, G. Tao, C. Zhou and G. K. Housley, *Journal of Power Sources*, **297**, 90 (2015).
8. G. Corre and A. Brisse, *ECS Transactions*, **68**, 3481 (2015).
9. J. Schefold, A. Brisse and H. Poepke, *Int. J. Hydrogen Energy* (2017).
10. G. Rinaldi, S. Diethelm, E. Oveisi, P. Burdet, J. Van herle, D. Montinaro, Q. Fu and A. Brisse, *Fuel Cells*, **17**, 541 (2017).
11. J. R. Mawdsley, J. David Carter, A. Jeremy Kropf, B. Yildiz and V. A. Maroni, *Int. J. Hydrogen Energy*, **34**, 4198 (2009).
12. Q. Fang, L. Blum and N. H. Menzler, *Journal of The Electrochemical Society*, **162**, F907 (2015).
13. Q. Fang, C. E. Frey, N. H. Menzler and L. Blum, *Journal of The Electrochemical Society*, **165**, F38 (2018).
14. P. Batfalsky, J. Malzbender and N. H. Menzler, *International Journal of Hydrogen Energy*, **41**, 11399 (2016).
15. N. H. Menzler, D. Sebold and O. Guillon, *Journal of Power Sources*, **374**, 69 (2018).

16. N. H. Menzler and P. Batfalsky, *Fuel Cell Science and Engineering: Materials, Processes, Systems and Technology*, Wiley-VCH (2012).
17. A. Mahmoud, M. Al Daroukh, M. Lipinska-Chwalek, M. Luysberg, F. Tietz and R. P. Hermann, *Solid State Ionics*, **312**, 38 (2017).
18. D. The, S. Grieshammer, M. Schroeder, M. Martin, M. Al Daroukh, F. Tietz, J. Schefold and A. Brisse, *Journal of Power Sources*, **275**, 901 (2015).
19. A. Mai, M. Becker, W. Assenmacher, F. Tietz, D. Hathiramani, E. Ivers-Tiffée, D. Stöver and W. Mader, *Solid State Ionics*, **177**, 1965 (2006).
20. N. H. Menzler, A. Beez, N. Grünwald, D. Sebold, Q. Fang and R. Vaßen, *ECS Transactions*, **78**, 2223 (2017).
21. A. Mahmood, S. Bano, J. H. Yu and K.-H. Lee, *Journal of Membrane Science*, **473**, 8 (2015).
22. N. H. Menzler, D. Sebold and E. Wessel, *Journal of Power Sources*, **254**, 148 (2014).
23. K. Chen and S. P. Jiang, *Journal of The Electrochemical Society*, **163**, F3070 (2016).
24. A. V. Virkar, *Int. J. Hydrogen Energy*, **35**, 9527 (2010).
25. A. Beez, X. Yin, N. H. Menzler, R. Spatschek and M. Bram, *Journal of The Electrochemical Society*, **164**, F3028 (2017).
26. P. Hjalmarsson, X. Sun, Y.-L. Liu and M. Chen, *Journal of Power Sources*, **262**, 316 (2014).
27. J. Laurencin, M. Hubert, D. F. Sanchez, S. Pylypko, M. Morales, A. Morata, B. Morel, D. Montinaro, F. Lefebvre-Joud and E. Siebert, *Electrochim. Acta*, **241**, 459 (2017).
28. F. S. Baumann, J. Fleig, G. Cristiani, B. Stuhlhofer, H.-U. Habermeier and J. Maier, *Journal of The Electrochemical Society*, **154**, B931 (2007).
29. J. Malzbender, P. Batfalsky, R. Vaßen, V. Shemet and F. Tietz, *Journal of Power Sources*, **201**, 196 (2012).
30. Y. Zheng, J. Wang, B. Yu, W. Zhang, J. Chen, J. Qiao and J. Zhang, *Chemical Society Reviews* (2017).
31. M. A. Laguna-Bercero, *Journal of Power Sources*, **203**, 4 (2012).
32. P. Moçoteguy and A. Brisse, *Int. J. Hydrogen Energy*, **38**, 15887 (2013).
33. E. Lay-Grindler, J. Laurencin, J. Villanova, P. Cloetens, P. Bleuet, A. Mansuy, J. Mougin and G. Delette, *Journal of Power Sources*, **269**, 927 (2014).
34. A. Hauch, S. D. Ebbesen, S. H. Jensen and M. Mogensen, *Journal of The Electrochemical Society*, **155**, B1184 (2008).
35. W. Schafbauer, *Entwicklung und Herstellung von foliengegossenen, anodengestützten Festoxidbrennstoffzellen*, Schriften des Forschungszentrums Jülich, Energy and Environment Vol. 66, Jülich (2010), available in German only.
36. M. B. Mogensen, A. Hauch, X. Sun, M. Chen, Y. Tao, S. D. Ebbesen, K. V. Hansen and P. V. Hendriksen, *Fuel Cells*, **17**, 434 (2017).
37. K. Zheng and M. Ni, *Science Bulletin*, **61/1**, 78 (2015).
38. B. Iwanschitz, D*egradation von Ni-Cermet Anoden in keramsichen Hochtemperatur-brennstoffzellen*, PhD thesis, RWTH Aachen (2012); available in German only.